論文 / 著書情報
Article / Book Information

Title	Biomimetic Realization of a Robotic Penguin Wing: Design and Thrust Characteristics
Authors	Yayi Shen, Natsuki Harada, Sho Katagiri, Hiroto Tanaka
Citation	IEEE/ASME Transactions on Mechatronics, Volume 26, Issue 5,
Pub. date	2020, 11
Copyright	(c) 2020 IEEE. Personal use of this material is permitted. Permission from IEEE must be obtained for all other uses, in any current or future media, including reprinting/republishing this material for advertising or promotional purposes, creating new collective works, for resale or redistribution to servers or lists, or reuse of any copyrighted component of this work in other works.
DOI	http://dx.doi.org/10.1109/TMECH.2020.3038224
Note	This file is author (final) version.

Biomimetic Realization of a Robotic Penguin Wing: Design and Thrust Characteristics

Yayi Shen, Natsuki Harada, Sho Katagiri, and Hiroto Tanaka

***Abstract*—Flapping flippers or fins are widely employed in biomimetic and bioinspired aquatic robots that imitate natural swimmers such as fish and dolphins. This paper involves robotic biomimetics of the penguin, which is often overlooked as an excellent swimmer benefiting from agile wings. To achieve equivalent swimming skills in an aquatic robot, the wing motion of a real penguin was investigated. Based on the findings, we developed a three-degree-of-freedom (3-DoF) robotic penguin wing that is able to implement the same flapping, feathering and pitch motions as in natural penguins. A kinematic analysis is presented, and the generation of swimming motions is demonstrated. We designed experiments to study the thrust characteristics of the motion of each joint. The results suggest that the flapping motion generates the main thrust during locomotion and the pitch angle can effectively change the thrust direction, while the feathering motion enables active control of the angle of attack (AoA). According to the results, stalling of the wing occurs near an AoA of 10° in the steady state; however, the feathering motion can avoid the stall and boost the net thrust by a factor of up to 7 relative to the net thrust without active feathering. Furthermore, the introduction of the feathering motion reduces the torque required to actuate the flapping motion. The hydrodynamics of the wing in different flow states are also discussed.**

***Index Terms*—Robotic penguin wing, biomimetic aquatic robot, thrust characteristics, agile swimming.**

I. Introduction

AQUATIC robots and vehicles are becoming of great value and interest in carrying out tasks ranging from environmental monitoring and oceanic exploration to search and rescue, device maintenance, and military applications. In addition to traditional unmanned underwater vehicles with rotary propellers, great progress has been made in biomimetic and bioinspired underwater robots in the past two decades due to their superior performance in many respects, including energy efficiency, motion stability, maneuverability and noiseless motion [1]–[3]. Scientists and engineers have studied the swimming mechanics of natural swimmers and have accordingly developed many bioinspired and biomimetic aquatic robots. The main sources of inspiration for such work have included fish [4]–[12], marine mammals such as dolphins [13]–[15], cephalopods such as squid [16]–[18], and other invertebrates such as jellyfish [19]–[21]. The above fish- and dolphin-mimetic robots employed flapping wings for propulsion. Hydrodynamic studies indicated that the flapping wing generates unsteady flow patterns varying with the amplitude and frequency as well as the shape of the kinematics applied [22]. Fish may use this unsteady flow mechanisms to augment force production [23]. To improve the performance, additional parameters have been introduced to the flapping motion, such as adding spanwise flexibility [24], investigating extra degree-of-freedom [25], and employing non-sinusoidal angle of attack profile [22].

In this paper, we present a robotic penguin wing for underwater propulsion (as shown in Fig. 1). Penguins are wing-propelled diving birds inhabiting the Southern Hemisphere. Unlike other groups of birds, penguins have completely adapted to underwater swimming and have lost the ability to fly in the air. Comparing with fish and dolphins that propel mainly through single caudal fins, penguins are propelled by a pair of flapping wings [26], [27], which means wide ranges of force and torque could be generated through conducting independent control over each wing. Therefore, the penguin's double-wing configuration is potentially superior to the caudal-wing configuration in terms of agility. In biological studies, video loggers mounted on wild gentoo penguins demonstrates that penguins can execute agile maneuvers, such as prompt turning and high acceleration, during predation [28]. Other biologging studies have also reported that the speed-to-weight ratio in penguins is relatively high among breath-hold divers [29] and that the swimming speed in penguins likely minimizes the cost of travel (i.e., the power consumption per unit travel distance) [30]. Concerning the details of the wing kinematics and hydrodynamics, however, are largely unknown. Previously, two-dimensional (2-D) sideview motion analysis of penguins in forward swimming at aquariums suggested lift-based thrust generation by flapping with appropriate feathering (i.e., wing rotation around spanwise axis) [26], [27], [31]. In particular, feathering is important since it directly change AoA (angle of attack) of the wing which crucially affects the flow field around the wing so as to resultant forces. It has also been indicated that while a penguin is swimming, no thrust is contributed either by body or tail oscillations or by foot movements [26]. In other words, penguin wings are functionally versatile. Unlike fish and dolphins that mainly propel with their caudal fins and maneuver with the assistance of pectoral fins, penguins can realize both propelling and maneuvering, and even effective force control through active AoA, within one propulsor (i.e., the wing). However, the quantitative 3-D wing kinematics which is required for the design of the penguin-mimetic wing mechanism have never been revealed.

In the robotics field, a bionic penguin named "AquaPen-

This work was supported by a JSPS KAKENHI Grant-in-Aid for Scientific Research on Innovative Areas (JP18H05468). *(Corresponding author: Hiroto Tanaka.)*

The authors are with the Department of Mechanical Engineering, Tokyo Institute of Technology, Tokyo, 1528550 Japan. (e-mail: shen.y.af@m.titech.ac.jp; harada.n.ac@m.titech.ac.jp; katagiri1007@gmail.com; tanaka.h.cb@m.titech.ac.jp)

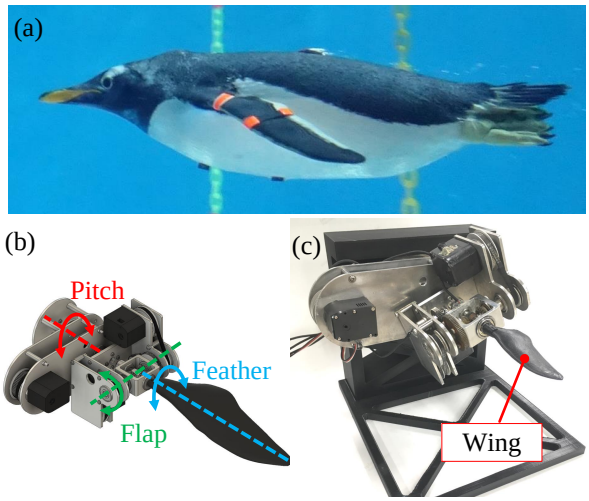

Fig. 1. (a) Gentoo penguin at Nagasaki Penguin Aquarium; (b) 3-D model of the robotic penguin wing; (c) prototype of the robotic penguin wing.

guin" was developed by FESTO ten years ago, where the wing actively flaps with a pre-fixed amplitude [32]. Feathering, however, was realized by passive deformation of the wing and not actively controlled. Another research proposed a spherical parallel mechanism to work as an animal (penguin, for instance) shoulder [33]. It can realize arbitrary three-degree-of-freedom (3-DoF) wing motion within a cone of 120° apex angle. Nevertheless, the universality of this mechanism sacrifices the capability of large flapping amplitude and compactness [34]. Among the previous fish- and dolphin-mimetic robots, most mechanisms generate main thrusts through flapping their caudal fins without feathering [4]–[6], [11]–[13]. But there is a fish-mimetic robot [5] and a dolphin-mimetic robot [14] that have realized feathering motion in their pectoral fins. However, they are separated with the flapping caudal fins and are mainly used for orientation adjustment. In a turtle-mimetic robot driven by shape-memory-alloy actuators, researchers added torsional motion into the flapping flipper, which is similar with the feathering motion in penguins [35]. It turned out the twist did help increase the thrust. Yet, the low actuation frequency up to 0.25 Hz limited the thrust generation and mechanisms underlying the torsional motion were not illustrated. To sum up, there still does not exist a single propulsor that can implement control on thrust magnitude with active AoA and thrust direction at the same time, let alone achieving penguin-like agile swimming.

This paper first presents the 3-D motion measurements of a real penguin in forward horizontal swimming to reveal the quantitative wing kinematics. Based on the results, a 3-DoF robotic penguin wing that is capable of actively controlling flapping and feathering angles and flapping direction was designed and created. The detailed actuation mechanism and fabrication method are introduced. The kinematics and generated swimming motion are also explained. Then, the ability of the robotic wing to control the thrust magnitude by active change of feathering and the thrust direction by active change of flapping direction was evaluated by water tunnel experiments. Finally, the hydrodynamic scalability of the robotic penguin wing is also discussed.

The principal contributions of this paper are as follows.

1) Performed 3-D motion measurements on a real penguin and revealed the 3-D wing kinematics.
2) Developed a penguin-wing-like propulsor that integrates active control on flapping and feathering angles and flapping direction simultaneously.
3) Verified the ability of the robotic penguin wing to effectively control the thrust magnitude by active change of feathering and the thrust direction by variation of flapping direction.

The remainder of this paper is organized as follows: In Section II, we present fundamental 3-D motion measurements of a real penguin wing during swimming. The design of penguin-mimetic wing mechanism and the kinematics are introduced in Section III. Then, the thrust evaluation method is explained in Section IV. In Section V, we present the experimental results, followed by related discussions on the hydrodynamic performance of the penguin-mimetic wing mechanism in Section VI. Finally, we summarize the current research and present an outline of future work.

II. Wing-Propelled Penguin Swimming

As mentioned in previous section, forward swimming of penguins was two-dimensionally recorded by researchers using laterally oriented high-speed cameras more than 30 years ago [26], [31], [36]. Although those studies yielded several valuable insights, such as the acceleration during upstrokes and downstrokes and the occurrence of wing deformation in large species, the ability to reveal the fluid dynamics mechanism by which wings generate hydrodynamic forces requires accurate 3-D measurements of the wing and body motions. Moreover, the behaviors and mechanisms underlying maneuvers such as turning have remained completely unknown.

To reveal quantitative wing kinematics in penguins, we performed 3-D motion measurements using multiple underwater video cameras at an aquarium. A gentoo penguin (*Pygoscelis papua*) with a weight of 7 kg and length of 0.7 m in swimming attitude (as shown in Fig. 1(a)) was selected as the research subject. We analyzed 7 wingbeats from 5 sequences of forward horizontal swimming at a nearly constant speed of 1.19 m/s (SD: 0.12). By comparison, a previous biologging study has reported that the average swimming speed of penguins during foraging in a wild ocean environment is 2.3 m/s [30]. As

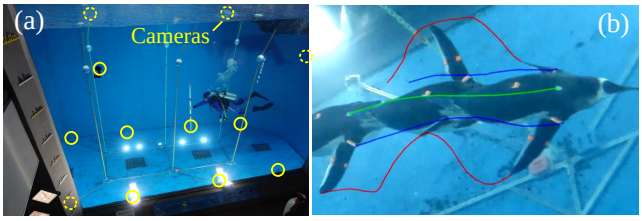

Fig. 2. (a) Field of the 3-D motion measurement in the aquarium; (b) example trajectories of the front dorsal marker (green line), the wing base markers (blue lines) and the wing tips (red lines) during one wingbeat (frequency: 1.82 Hz; swimming speed: 1.32 m/s).

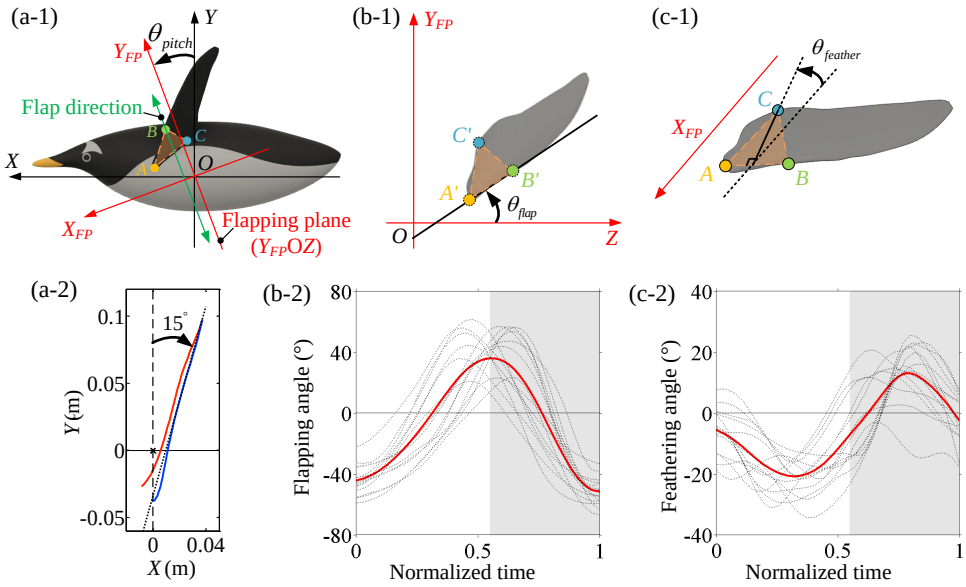

Fig. 3. Definitions and ranges of the penguin wing motions: (a-1) definition of pitch of the flapping plane and (a-2) the 3-D measurement result (red line indicates trajectory of leading edge marker during upstroke, blue line indicates downstroke); (b-1) definition of flapping angle and (b-2) measured flapping angle range; (c-1) definition of feathering angle and (c-2) measured feathering angle range.

shown in Fig. 2(a), the water tank at the aquarium is 14 m in length, 4 m in width, and 4 m in depth. Twelve waterproof cameras (GoPro HERO6 Black, with a resolution of 3840 $\times$ 2160 pixels, a frame rate of 60 fps, and an exposure time of 1/480 s) were mounted in the water tank (marked with yellow circles in the figure, solid ones indicate visible cameras, dotted ones indicate invisible cameras), and ten markers for motion analysis were attached to the penguin: 2 dorsal markers, 2 ventral markers, and 3 wing markers on each wing. The trajectories of three selected markers during one wingbeat were depicted in Fig. 2(b) to show the general swimming motion. The 3-D positions were calculated using motion analysis software (DIPP-motion V/3D, Ditect, Japan). Note that in this paper, we focus on the three orange wing markers as seen in Fig. 1(a) for wing motion investigation. Further details of the experimental methods and the results of the motion analysis will be presented in another paper.

As a result, it was found that the basic wing kinematics relative to the body consists of obliquely straight flapping with spanwise feathering. Thus, we decomposed the wing motions of the penguin into three DoFs: flapping, feathering and pitch, as depicted in the top of Fig. 3. As shown in Fig. 3(a-1) of the side view of the penguin, the inertial frame O-XYZ is fixed with respect to the penguin's body, with the X-, Y-, and Z-axes corresponding to the surge, heave, and sway translational directions, respectively. Z axis goes through origin O and comes outside of the paper vertically. Three points on the wing indicate the locations of the wing markers, which to be specifically, point A as the wing root marker, point B as the leading edge marker and point C as the trailing edge marker. The three markers also define the wing plane ABC. To define the pitch DoF and the flapping DoF which corresponds to the main oscillating motion of the penguin wing, we first introduce the flap direction and the flapping plane. Flap direction is determined by the top and bottom positions of the leading edge marker B, as depicted in green color. Then coordinate O-$X_{FP}Y_{FP}Z$ (named flap coordinate) is defined so that plane $Y_{FP}OZ$ (named flapping plane) is parallel to the flap direction. As a result, pitch angle (θ_{pitch}) is the angle between the flapping plane $Y_{FP}OZ$ and the Y-axis. To obtain the flapping angle, wing axis which connects the wing root marker A and the leading edge marker B is projected on the flapping plane as shown in Fig. 3(b-1). Points $A^{'}$, $B^{'}$ and $C^{'}$ are the projected points. Flapping angle θ_{flap} is thus the angle between the projected wing axis (line $A^{'}B^{'}$) and the Z-axis. As for the feathering angle $\theta_{feather}$, it is a rotational angle of the wing plane ABC around the wing axis AB as shown in Fig. 3(c-1). When $\theta_{feather}$ is zero, the wing plane is parallel to the X_{FP}-axis. While positive $\theta_{feather}$ indicates pronation and negative $\theta_{feather}$ indicates supination.

To determine the motion ranges, the results of the 3-D motion measurements are shown in the bottom of Fig. 3. Fig. 3(a-2) depicts the trajectory of the leading edge marker B during upstroke (red line) and downstroke (blue line), which turns out the average pitch angle is around 15°. This positive pitch presumably generates downward thrust balancing the buoyancy. Fig. 3(b-2)(c-2) show the results of flapping motion and feathering motion, where the black lines represent the directly observed data from the wingbeats and the red lines represent the ensemble average values. The upstrokes and downstrokes of the wingbeats are distinguished by white and gray backgrounds, respectively. Based on the measurement results, it is found that the flapping motion and feathering motion follow almost sinusoidal curves. The average amplitudes of the corresponding angles are 40° and 20°, respectively. Moreover, the phase of the feathering motion is almost $\pi/2$ behind that of the flapping motion. Bear in mind that the above wing kinematics may change with other maneuvers such as turning

or ascending/descending. Specific wing kinematics for those maneuvers will need more investigations.

III. Robotic Penguin Wing

The previous section provides a preliminary overview of the swimming motion of a real penguin wing. According to the definition of each motion, we believe that the flapping motion generates the main propelling thrust while the penguin is swimming, whereas the pitch angle of the flapping plane serves to alter the thrust direction. Meanwhile, the feathering motion plays an important role in changing the angle of attack between the wing and the water inflow, which can result in a large variance in the generated thrust. To verify the specific swimming motions in the penguin and realize equivalent swimming skills, a robotic penguin wing has been developed; its design is explained in this section.

A. Wing Fabrication

To imitate a real penguin wing and achieve comparable swimming performance, a portable non-contact 3-D scanner (Space Spider, Artec3D) was applied to measure the 3-D profile of the wing of a living gentoo penguin, which is the same individual as in the kinematics measurement. As shown in Fig. 4(a), the inertial coordinate is same as defined in the previous section. To measure the size the of the wing, wing tip (point D) is introduced so that points A, B, C, D are on the same surface. Moreover, segment AD that connects the wing root and the wing tip is adjusted to be vertical to the X-axis. The actual wing length l_0 (maximum length along the spanwise direction) of the selected penguin was measured to be 252 mm, and the projected wing area S_0 is 14110 mm^2. Then, the average chord length w_0 can be calculated as $w_0 = S_0/l_0$. In the original scanned data, the cross-sectional profiles of the wing are almost symmetric, as seen in Fig. 4(b). This symmetric profile matches with the previous report of wing dissection for three penguin species including the gentoo penguin [27]. For simplicity, we modified these profiles to be completely symmetric and eliminated any spanwise torsion and bending. Accordingly, a rigid wing was fabricated with a 3-D printer (Ultimaker S5, Ultimaker B.V., Netherlands) using polylactide (PLA) material, as shown in Fig. 4(c). Although the real wing presumably undergoes a certain level of passive deformation during flapping, the rigid wing enables extraction of clear relationship between the wing motion and hydrodynamic performance eliminating the effect of wing deformation in the following experiments. Considering the size requirements in the following water tunnel experiments, a 0.4-scale wing was adopted. To ensure the similarity of wing kinematics and hydrodynamics with the real penguin, two dimensionless quantities (St, Re) will be introduced in the following sections. The details of the fabricated wing can be found in Table I.

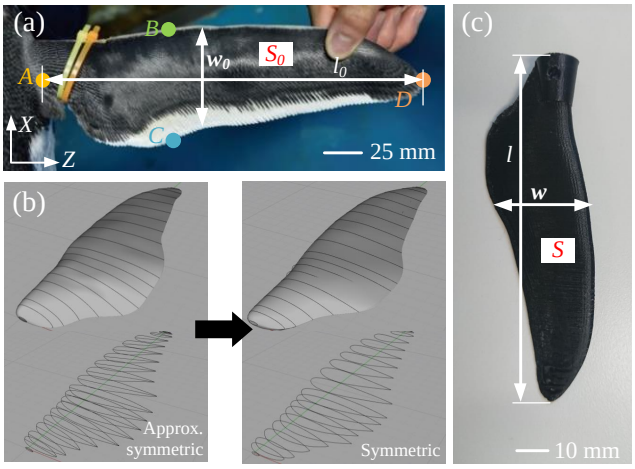

Fig. 4. (a) Wing of a gentoo penguin; (b) 3-D model of the wing created from the scanner data; (c) printed 0.4-scale model relative to the real penguin wing.

TABLE I
SPECIFICATIONS OF THE FABRICATED WING

Description	Value
Material	Tough PLA
Mass	8.7 g
Area (S)	2256 mm^2
Wing length (l)	101 mm
Average chord length (w)	22.3 mm
Maximum thickness	6 mm

B. Driving Mechanism

The driving mechanism is composed of two main parts, as shown in Fig. 5(a). The differential gear part contains three bevel gears to realize differential actuation of the wing. Two servo motors (1 and 2) actively control the rotation of two of the bevel gears (1 and 2). As a result, the wing can perform flapping and feathering motions. The other part of the driving mechanism is the base part, which is to be fixed on the robot's body in the future. It controls the pitch motion of the differential part and the wing. To obtain the instantaneous angular positions of the flapping, feathering and pitch motions for accurate control, three potentiometers (blue blocks shown in Fig. 5(a)) are installed at each end of the transmission for direct feedback. In summary, there are three actively controlled joints in the robotic penguin wing mechanism: motor 0 controls the pitch of the flapping plane, and motor 1 and motor 2 control the rotation of bevel gear 1 and bevel gear 2, respectively. The angular velocities of the pitch motion, gear 1 and gear 2 are denoted by ω_0, ω_1 and ω_3, respectively. According to the kinematics of the differential gear system (as shown in Fig. 5(b)), the angular velocities of revolution and rotation of bevel gear 3 can be calculated as follows:

$$\begin{cases} \omega_{3\alpha} = \dfrac{\omega_1 + \omega_2}{2} \\ \omega_{3\beta} = \dfrac{\omega_1 - \omega_2}{2} \end{cases} \tag{1}$$

where $\omega_{3\alpha}$ denotes the revolution velocity of bevel gear 3 around the X_W-axis and $\omega_{3\beta}$ denotes the rotation velocity

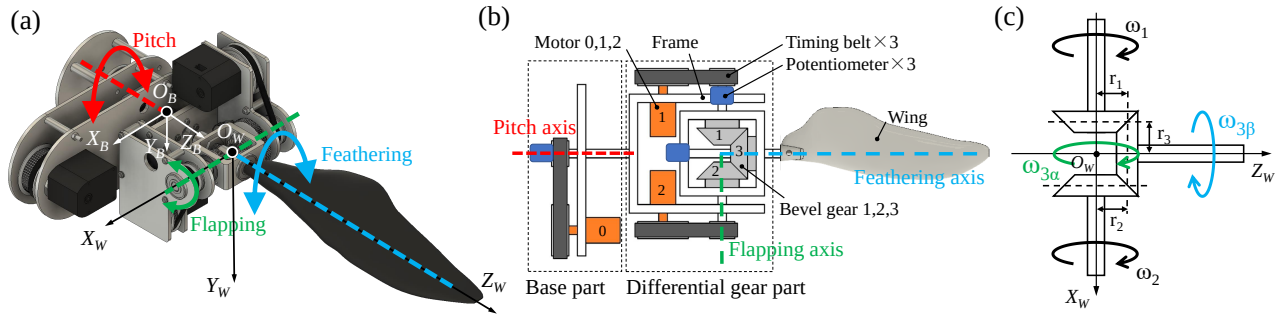

Fig. 5. (a) Driving mechanism of the robotic penguin wing; (b) schematic drawing of the differential gear mechanism for realizing the flapping and feathering motions; (c) coordinate systems and 3-DoF motion realized in the robotic penguin wing.

of bevel gear 3 around the Z_W-axis. The pitch radii of the bevel gears (r_1, r_2, and r_3) are designed to be the same. Since bevel gear 3 is fixed and relatively static with the wing, the revolution and rotation angles of bevel gear 3 are actually equal to the flapping and feathering angles of the wing. Hence, the relation between the input velocities (ω_0, ω_1, and ω_2) and the output velocities (ω_{pitch}, ω_{flap}, and $\omega_{feather}$) can be rewritten in matrix form as follows:

$$\begin{bmatrix} \omega_{pitch} \\ \omega_{flap} \\ \omega_{feather} \end{bmatrix} = \begin{bmatrix} 1 & 0 & 0 \\ 0 & \frac{1}{2} & \frac{1}{2} \\ 0 & \frac{1}{2} & -\frac{1}{2} \end{bmatrix} \begin{bmatrix} \omega_0 \\ \omega_1 \\ \omega_2 \end{bmatrix} \tag{2}$$

Notably, there is a timing belt transmission between each motor and the input driving shaft, which leads to a proportional difference between the motor velocity and the driving shaft velocity. This driving mechanism can achieve arbitrary motion of flapping, feathering and pitch in angular ranges from -90° to 90°, which is much larger than the previous penguin-mimetic joint mechanism (i.e., from -60° to 60°) [33] and is sufficient for most flapping trajectories found in nature.

The definitions of the coordinate systems are shown in Fig. 5(c), which is different from that in the motion measurements of the real penguin (Fig. 3). The origin of the body frame O_B-$X_BY_BZ_B$ (F_B) is fixed at the base part, and the X_B-axis is in the forward direction, the Z_B-axis is aligned with the rotational shaft (red dashed line) for the pitch motion. The wing frame O_W-$X_WY_WZ_W$ (F_W) is always fixed with the wing, in which, the X_W-axis lies along the flapping shaft (green dashed line), and the Z_W-axis lies along the feathering shaft (blue dashed line). Origin O_W locates at the intersection point of flapping axis and feathering axis, which is at the center of the bevel gears. The rotational transformation matrix from the inertial frame (F_B) to the wing frame (F_W) is based on the three kinds of wing motion and can be written as follows:

$$R_W^B = R(\theta_{pitch})R(\theta_{flap})R(\theta_{feather}) \tag{3}$$

where $R(\theta_{pitch})$, $R(\theta_{flap})$, and $R(\theta_{feather})$ denote the rotational matrices resulting from the pitch, flapping and feathering motions, respectively. Specifically,

$$\begin{cases} R(\theta_{pitch}) = \begin{bmatrix} \cos(\theta_{pitch}) & -\sin(\theta_{pitch}) & 0 \\ \sin(\theta_{pitch}) & \cos(\theta_{pitch}) & 0 \\ 0 & 0 & 1 \end{bmatrix} \\ R(\theta_{flap}) = \begin{bmatrix} 1 & 0 & 0 \\ 0 & \cos(\theta_{flap}) & -\sin(\theta_{flap}) \\ 0 & \sin(\theta_{flap}) & \cos(\theta_{flap}) \end{bmatrix} \\ R(\theta_{feather}) = \begin{bmatrix} \cos(\theta_{feather}) & -\sin(\theta_{feather}) & 0 \\ \sin(\theta_{feather}) & \cos(\theta_{feather}) & 0 \\ 0 & 0 & 1 \end{bmatrix} \end{cases} \tag{4}$$

where the posture angles θ_{pitch}, θ_{flap} and $\theta_{feather}$ can be calculated through the integration of the angular velocities in Equation 2.

C. Angle of Attack (AoA)

In fluid dynamics, there is another crucial parameter called the angle of attack (AoA), which affects the flow pattern and consequently influences the thrust performance. Fig. 6(a) shows the definition of the AoA for the robotic penguin wing. Considering a random point A on the Z_W-axis, let the vector of point A on the wing be

$$\boldsymbol{r}^W = \begin{bmatrix} 0 \\ 0 \\ r_z \end{bmatrix} \tag{5}$$

Then, the velocity of this point in the body frame can be obtained as follows:

$$\boldsymbol{v}_r^B = \frac{\mathrm{d}\boldsymbol{r}^B}{\mathrm{dt}} = \frac{\mathrm{d}((R_W^B)^{-1}\boldsymbol{r}^W)}{\mathrm{dt}} \tag{6}$$

If the instantaneous swimming velocity of the robot's body is $\boldsymbol{v}_b^B$, then the relative velocity, or inflow velocity, at point A can be derived as follows:

$$\boldsymbol{v}_{in}^B = -(\boldsymbol{v}_r^B + \boldsymbol{v}_b^B) \tag{7}$$

As shown in Fig. 6(a), the angle α between the inflow vector ($\boldsymbol{v}_{in}^W$) and the wing plane ($X_WO_WZ_W$) is then defined as the AoA, which also equals the angle between the inflow vector and the chord line. The chord line goes through point A and aligns with the projection of the inflow vector on the wing

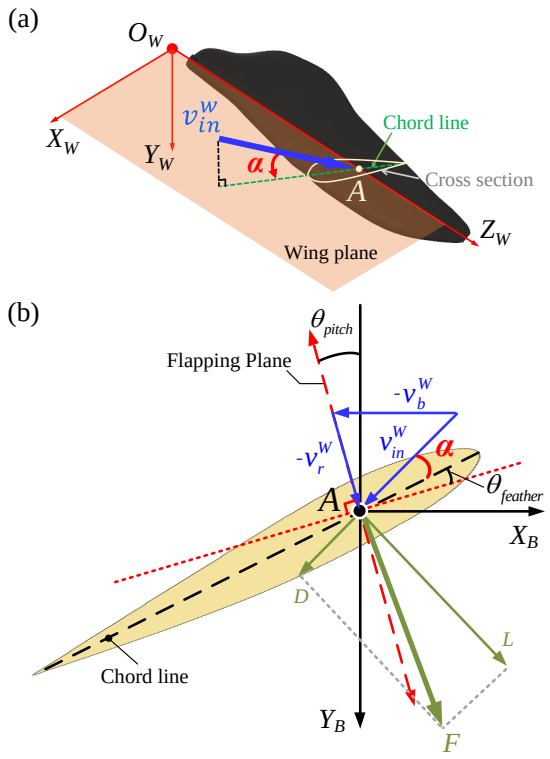

Fig. 6. Definition of the AoA for the robotic penguin wing: (a) general situation in a 3-D view; (b) analysis on the cross section when $\theta_{flap} = 0$.

plane. The AoA can be calculated as

$$\alpha = -\arctan\left(\frac{v_{in,y}^W}{\sqrt{(v_{in,x}^W)^2 + (v_{in,z}^W)^2}}\right) \tag{8}$$

Therefore, the value of the AoA is dependent on many factors, including the wing motion, the location of the selected point and the swimming velocity. For simplicity, we choose a typical representative point A, which is located at 75% of the whole wing length from the wing base on the Z_W-axis, for the calculation of the AoA.

To illustrate how the AoA is affected by the three kinds of wing motions so as to result in generating different hydrodynamic forces, analysis on the cross section of the wing are made. The cross section passes through the chord line and is parallel to the Y_W-axis. In Fig. 6(b), we consider a moment at which the flapping angle (θ_{flap}) is zero but both the pitch angle (θ_{pitch}) of the flapping plane and the feathering angle ($\theta_{feather}$) of the wing plane are nonzero. In addition, we consider that the swimming velocity of the robot lies only in the X_B direction. The visual angle of the cross section is from the $-Z_W$ direction in Fig. 6(a). $-\boldsymbol{v}_b^W$ and $-\boldsymbol{v}_r^W$ denote the flow velocity caused by the motion of the robot's body and the motion of the wing flapping, respectively. Hence, the angle between the inflow velocity ($\boldsymbol{v}_{in}^W$) and the chord line is the AoA (α). It can be easily seen that a larger feathering angle ($\theta_{feather}$) leads to a smaller AoA (α). According to fluid dynamics, the lift force ($\boldsymbol{L}$) and drag force ($\boldsymbol{D}$) are defined as the components of the resultant force $\boldsymbol{F}$ that are perpendicular and parallel, respectively, to $\boldsymbol{v}_{in}^W$, which also means that

$$\boldsymbol{F} = \boldsymbol{L} + \boldsymbol{D} = \boldsymbol{F}_x^B + \boldsymbol{F}_y^B \tag{9}$$

where $\boldsymbol{F}_x^B$ and $\boldsymbol{F}_y^B$ are the force components in the X_B and Y_B directions, respectively. Therefore, a larger lift-to-drag ratio may produce a greater effective thrust in the X_B direction. In particular, the lift force increases linearly with the AoA before stall (i.e., the separation of the flow from the wing) but starts to decrease after stall. Since the feathering angle can be modified to realize adjustment of the AoA, the thrust performance of the robotic penguin wing may be improved and actively controlled in this way.

IV. Method of Evaluating Thrust Characteristics

To realize motion control over a penguin-like robot, thrust characteristics of the wing should be clarified first. In this paper, thrust characteristics of the robotic penguin wing are evaluated in terms of thrust force to illustrate the effect of each joint. We designed a series of swimming motions to allow us to analyze the thrust from various perspectives, including the thrust amplitude, the thrust direction, and how the newly introduced feathering angle affects propulsion. An experimental platform has also been developed to measure the thrust force generated by the robotic penguin wing in a water tunnel during all types of motion.

A. Experimental Setup

Fig. 7(a) shows the overall control structure of the experimental setup, which consists of four parts. The PC issues high-level commands such as flapping, feathering and pitch motion commands. These commands are then converted into velocities for each joint through kinematics. The PID controller for the joint velocity is realized in a microcontroller unit (MCU) and is used to actuate the wing mechanism to follow the desired motion. As mentioned in Section III(B), three potentiometers are used to provide direct feedback on the posture angles of the flapping, feathering and pitch motions. To measure the thrust generated by the wing motion, a 6-axis force/torque sensor is connected to the robotic penguin wing. The data of both the posture angles and the measured forces are acquired by a DAQ card at a sampling frequency of 1000 Hz. Automatic wavelet noise reduction is applied to process the sample noise [37].

Photographs of the experimental platform and the control desk are provided in Fig. 7(b)(c). A water tunnel with a maximum flow speed of 2 m/s and measuring 1 m $\times$ 0.2 m $\times$ 0.3 m was used in the experiments. The robotic penguin wing was adjusted to an appropriate position in the tunnel to avoid disturbance from the walls. The test section was closed except for a hole for the robot to reduce the effect of the free surface. To ensure that the thrust could be measured effectively, the wing part was always submerged under the surface of the water during motion, while the motors were above the water surface. The whole robotic penguin wing, including the motors and the transmission mechanism, was mounted below the force sensor, whose axes are depicted in the figure. It is also seen that the wing was vertically inserted in the water tunnel. The output of the force sensor was set to be zero before applying flow and

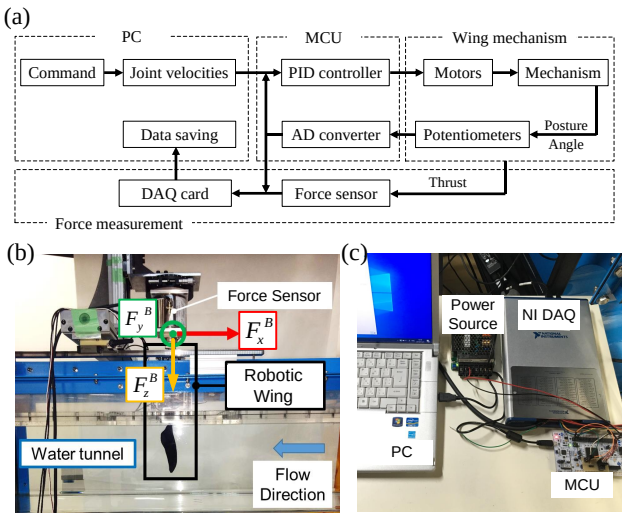

Fig. 7. (a) Control structure of the experimental setup; (b) photograph of the experimental platform; (c) photograph of the control desk.

TABLE II
DEVICES USED IN THE EXPERIMENTAL SETUP

Device	Model
Water tunnel	PT-100, West Japan Fluid Engineering Lab, Japan
PC	64-bit Windows, 3.30 GHz, USA
MCU	Nucleo-144, STMicroelectronics, Switzerland
Motor	KRS-4032HV (max. 1.94 Nm), KONDO, Japan
Potentiometer	P13SM, Vishay Intertechnology, USA
Force sensor	SFS080 (max. 50N), Leptrino, Japan
DAQ card	NI USB-6343, National Instruments, USA

starting experiments, thus gravitational force does not affect the measurements. Table II lists the devices used in the thrust measuring setup.

B. Motion Generation

We generated the motion for each joint based on the 3-D measurements of the real penguin wing during swimming presented in Section II. The trajectories of the flapping and feathering motions were sinusoidal to realize cyclical, smoothly oscillating movements, while the pitch angle was set to be constant to explore the exact relation with respect to the thrust direction. Hence, the angular position of each joint in the robotic penguin wing could be expressed as follows:

$$\begin{cases} \theta_{flap} = A_{flap}\sin(2\pi ft) \\ \theta_{feather} = A_{feather}\sin(2\pi ft - \dfrac{\pi}{2}) \\ \theta_{pitch} = A_{pitch} \end{cases} \tag{10}$$

where A_{flap} and $A_{feather}$ are the amplitudes of the flapping and feathering motions, respectively. The oscillation frequencies of flapping and feathering were both set equal to f to ensure motion consistency. In addition, the phase of the feathering motion was set to be $\pi/2$ behind that of the flapping motion, in accordance with the measurement results (see Fig. 3).

C. Parameter Settings

To ensure the similarity of wing kinematics and hydrodynamics with the real penguin, two dimensionless quantities were employed for determining the experimental parameters. One is the Strouhal number (St) which represents unsteadiness of flapping motion relative to the main flow (i.e. forward swimming velocity), and another is the Reynolds number (Re) which represents similarity of flow field. Ideally, St and Re should be kept the same with those of real penguins during experiments. Due to the size and flow speed limitations of our water tunnel, however, St and Re cannot be guaranteed simultaneously. Therefore, we set St to be similar, while verified the Re to be in the same order of magnitude to ensure the similarity.

The Strouhal number (St) is defined as

$$St = \frac{fL}{U} \tag{11}$$

where f is the motion frequency, U is the flow speed, and L denotes the flapping amplitude in units of length at the wing tip, which can be calculated by

$$L = 2l\sin(A_{flap}) \tag{12}$$

where A_{flap} denotes the flapping amplitude and l denotes the wing length. Interestingly, it has been found that many aquatic and aerial animals swim or fly within a certain range of St (e.g., $0.2 < St < 0.4$) to achieve high locomotory efficiency [38]. In our experiments, a constant St was decided based on the measurement of real penguins. Hydrodynamically speaking, we attempt to simulate the forward swimming of a wild foraging penguin in the Antarctic Ocean with the average flapping amplitude of 40° according to our measurement, flapping frequency of 2.18 Hz and swimming speed of 2.3 m/s according to a previous report [30]. These conditions result in a St of 0.26 and a Re in the range of $6.7\times10^4 \sim 9.8\times10^4$ assuming a water temperature of 0°C. As introduced in Section III.A and IV.A, a 0.4-scale wing was employed to minimize the effect of the walls of the water tunnel. To maintain a similar St, meanwhile, prevent reduction of Re as much as possible, flapping amplitude was kept the same as 40°, flapping frequency was set as 2.2 Hz and flow speed was set as the maximum of 1 m/s. Note that the possible maximum speed of our water tunnel is 2 m/s, nevertheless, the flow near the opening of the water tunnel fluctuates seriously after 1 m/s.

These operation conditions resulted in a St of 0.277 which is very close to the real penguin situation (0.26); and a Reynolds number (Re) in the range of $2.4\times10^4 \sim 3.2\times10^4$, which is in the same order of magnitude with real penguin. The Re is defined as

$$Re = \frac{\rho\,|v_{in}|\,w}{\mu} \tag{13}$$

where ρ represents the density of the fluid, v_{in} represents the relative flow speed as defined in (7), w is the average chord length of the wing and μ is the viscosity of the fluid. In our case, the water temperature was controlled by the water tunnel to be constantly 25°C, leading to a density of 997 kg/m^3 and a viscosity of 8.9×10^{-4} Pa·s.

As listed in Table III, all trials were divided into two sets.

TABLE III
EXPERIMENTAL TRIALS

Trial Set	Parameter Description	Symbol	Value	*St*	*Re*
Set 1	Flapping amplitude (frequency)	A_{flap} (f)	30° (2.8 Hz), 40° (2.2 Hz), 50° (1.8 Hz)	0.277	24000 ≀ 32000
	Feathering amplitude	$A_{feather}$	0°, 5°, 10°, 15°, 20°, 25°, 30°, 35°, 40°		
	Pitch angle	A_{pitch}	0		
	Flow speed of water tunnel	U	1 m/s		
Set 2	Flapping amplitude (frequency)	A_{flap} (f)	30° (2.8 Hz), 40° (2.2 Hz), 50° (1.8 Hz)		
	Feathering amplitude	$A_{feather}$	20°		
	Pitch angle	A_{pitch}	−20°, −15°, −10°, −5°, 0, 5°, 10°, 15°, 20°		
	Flow speed of water tunnel	U	1 m/s		

The first set explored how the feathering motion affects the thrust amplitude, so the pitch angle was set to zero. The purpose of the second set was to study how the pitch angle generates vectored thrusts; hence, we maintained a constant feathering angle which was set equal to the optimal result from the first set, and varied the pitch angle. In both sets, we varied the flapping amplitude to investigate how it affects the thrust amplitude. Since the average flapping amplitude in penguins is approximately 40°, we set the flapping amplitude to three different values (30°, 40°, and 50°) to compare the different possible thrust amplitudes. Accordingly, motion frequency was set to 2.8 Hz, 2.2 Hz, and 1.8 Hz to keep *St* constant. Similarly, the feathering amplitude was increased from 0° to 40° in intervals of 5°, and the pitch angle was varied from −20° to 20° with the same interval size, which were determined based on the average values obtained in the measurements. Note that the amplitude of v_{in} in (13) was almost constant since both *St* and U were constant in our experiments. Hence, the resultant range of *Re* was also nearly the same.

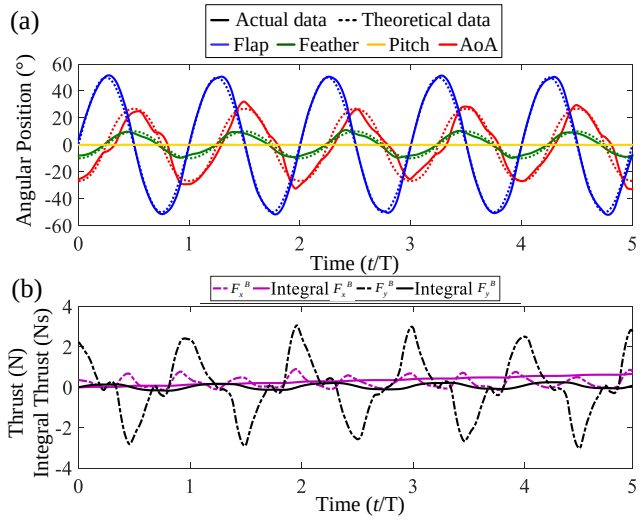

Fig. 8. (a) Time histories of the flapping angle, feathering angle, pitch angle and AoA with $A_{flap} = 50°$, $A_{feather} = 10°$, and $A_{pitch} = 0$; (b) instantaneous and integral thrust forces in X_B and Y_B directions throughout five periods.

V. Experimental Results

A. Effect of Feathering on Thrust Generation

The first set of trials in Table III were conducted to explore the effect of direct control of the AoA by feathering on thrust in the forward direction. All the trials were repeated three times, and in each trial the middle five motion periods were extracted for analysis to avoid unstable flow effects. In Fig. 8(a), the angular position of each joint throughout five motion periods ($5T$) with $A_{flap} = 50°$, $A_{feather} = 10°$, and $A_{pitch} = 0$ is presented as an example. The AoA was also calculated with (8) and is depicted in the figure. While the measured flapping and feathering angles well follow the theoretical values, there are notable discrepancies on the AoA, particularly around the beginning of each stroke. This is assumed to be due to the slight delay of flapping, that decreases the flapping velocity and resultant AoA amplitude (Fig. 6 and (8)). Nonetheless, all the measured angles generally follow the trends and amplitudes of the target values. The time histories of the measured instantaneous thrusts F_x^B and F_y^B during this trial are shown in Fig. 8(b) as dashed lines. The integrals of these instantaneous thrusts over time were also calculated and are depicted in the figure as solid lines. Although the amplitude of F_y^B is larger than that of F_x^B, the integrated thrust on the Y_B-axis is nearly zero due to the symmetric thrust profile. Hence, we focus on the thrust in the forward direction (X_B-axis) and study how the feathering angle affects the F_x^B performance. Fig. 8 shows that F_x^B reaches a peak when the wing flaps through the central position ($t = T/2$), corresponding to the fastest flapping velocity and the largest AoA. The amplitude of the peak varies with different flapping and feathering angles. To compare all investigated situations, Fig. 9(a) plots the maximum and minimum instantaneous thrusts generated during movement. At all flapping amplitudes, the maximum thrust initially increases with a larger feathering amplitude. However, it then starts to decrease after reaching an extreme point. The exact position of the extreme point depends on the flapping amplitude, but it is clear that the largest thrusts occur with feathering amplitudes ranging from 15° to 20°. In addition, we find that a smaller flapping amplitude A_{flap} with a higher frequency f generally leads to a larger instantaneous thrust in both the positive and negative directions. However, a larger flapping amplitude tends to reduce the negative thrust, which may result in a larger net thrust.

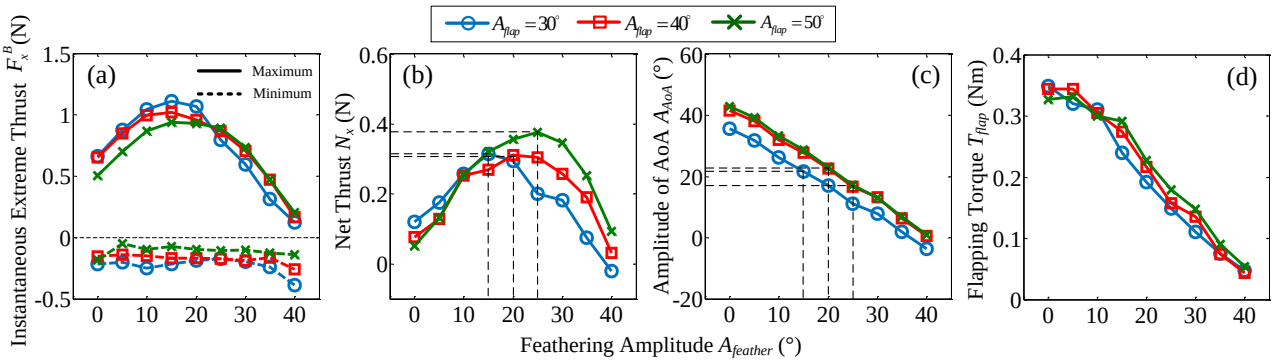

Fig. 9. Thrust characteristics with varying flapping and feathering motion parameters: (a) maximum and minimum instantaneous thrusts with different flapping and feathering angles; (b) net thrusts in all trials, with the extreme points marked; (c) AoAs corresponding to different flapping and feathering angles, with the points of maximum net thrust marked; (d) variations of the flapping torque amplitude with different feathering and flapping angles.

Considering the existence of both positive and negative thrust forces, the net thrust (N) was employed for evaluation. The net thrust is defined as

$$N_{x,y} = \frac{\int_0^{5T} F_{x,y}^B(t)\mathrm{dt}}{5T} \tag{14}$$

where $F_{x,y}^B(t)$ denotes the instantaneous force in the X_B or Y_B direction and $5T$ denotes the duration of the force measurements used for the calculation. The results are shown in Fig. 9(b). Similar to the instantaneous force, extreme points exist on the net thrust curves with respect to the feathering amplitude. Interestingly, at the specific St and in the corresponding range of Re used in these experiments, the combination of a larger flapping amplitude with a lower frequency allows a large net thrust to be more effectively generated with the capability of active feathering. The feathering amplitude that results in the largest net thrust varies with the flapping amplitude, being $A_{feather} = 15^\circ$ when $A_{flap} = 30^\circ$, $A_{feather} = 20^\circ$ when $A_{flap} = 40^\circ$, and $A_{feather} = 25^\circ$ when $A_{flap} = 50^\circ$ (marked with dashed lines). To explain this phenomenon, we plot the amplitude of the AoA with different feathering angles in Fig. 9(c). The AoA amplitude increases with a smaller feathering amplitude, which can be derived from Fig. 6(b) and (8). Moreover, we have marked the points at which the largest net thrusts are generated with dashed lines, from which it is easy to find that all of them correspond to AoAs near 20° (21.7°, 22.5°, 17.2°). As pointed out by previous researchers, the AoA plays an important role in generating an effective lift force in fluid dynamics. The lift force increases with an increasing AoA before the stall point and starts to decrease after the stall point. Based on our experimental results, we believe that stall occurs when the AoA is near 20°. In other words, the feathering motion of our robotic penguin wing can be controlled to maximize the effective thrust while avoiding stall. In addition, the maximum torque that is needed to realize the flapping motion (called the flapping torque) was calculated for various feathering amplitude situations, as shown in Fig. 9(d). The flapping torque T_{flap} can be obtained as follows:

$$T_{flap} = F_y^B d \tag{15}$$

where d is the moment arm from the flapping shaft (X_W) to the representative chord plane (i.e., 75% wing length from the base) that is defined in Section III(C). The results presented in this figure show that larger feathering angles are associated with smaller flapping torques, thus highlighting that the active control of the feathering angle not only increases the net forward thrust but also reduces the torque required to actuate the flapping motion.

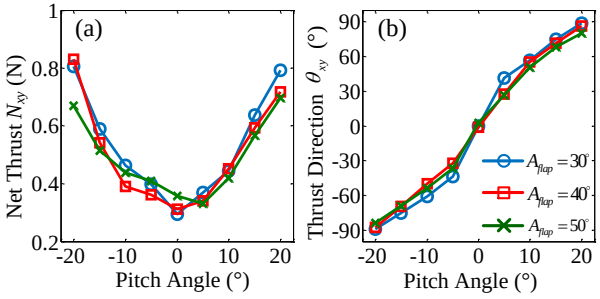

Fig. 10. Thrust characteristics with different flapping and pitch motions: (a) amplitude of the resultant thrust; (b) direction of the resultant thrust.

B. Effect of Pitch on Thrust Direction

To explore how the direction of the thrust can be controlled by pitch, the second set of trials in Table III were conducted with the robotic penguin wing. In this section, we inspect the simultaneous thrusts in the X_B and Y_B directions to determine the direction of the net thrust. As shown in Fig. 10, the pitch angle was set to be symmetric about zero, and the resulting generated net thrusts N_{xy} and directions θ_{xy} are also symmetric about the central position. These quantities can be calculated as follows:

$$\begin{cases} N_{xy} = \sqrt{N_x^2 + N_y^2} \\ \theta_{xy} = \arctan(\dfrac{N_y}{N_x}) \end{cases} \tag{16}$$

where N_x and N_y are the net thrusts in the X_B and Y_B directions, respectively. As shown in Fig. 10(b), the thrust direction varies almost linearly with the pitch angle. Moreover, a 40° variation in the pitch angle causes a 180° change in the resultant thrust direction, showing high efficiency of the direction control.

VI. Hydrodynamic Discussion

In this section, we compare the lift and drag coefficients from the flapping wing (i.e., unsteady state) and the fixed wing (i.e., steady transverse state) to discuss possible force enhancement effect. Previous fluid dynamics study simulating flapping-wing hovering of insects and hummingbirds demonstrated that the flapping wing can produce larger lift and drag coefficients than the traversing wing [39]. This effect of force enhancement was confirmed for the wide range of Re from 1.1×10^2 to 1.4×10^4, and suggested that possibly effective for larger Reynolds number. Therefore, the present penguin-mimetic wing mechanism may produce larger lift and drag coefficients than those of the steady fixed wing, that would enhance the ability to generate large thrust. The lift and drag coefficients, C_L and C_D, are expressed as follows:

$$\begin{cases} L = \frac{1}{2} C_L(\alpha) \rho v_{in}^2 S \\ D = \frac{1}{2} C_D(\alpha) \rho v_{in}^2 S \end{cases} \tag{17}$$

where the definitions of the parameters are the same as those in the previous sections. Both of these coefficients can be expressed as functions of α given the same Re and St. These functions of α also varies with the planar and cross-sectional shape of the wing.

To measure C_L and C_D for the steady case, the setup depicted in Fig. 7 was used while the wing was held to be still. The feathering angle was adjusted for different AoAs and fixed during the measurement. In all trials, the flow speed (U) of the water tunnel was adjusted to 1.2 m/s, corresponding to a Reynolds number of 2.67×10^4, which also falls within the Re range of the flapping-wing experiments. The force coefficients were then calculated based on the measured forces; the results are shown in Fig. 11 as red and blue dotted lines. Stall in lift occurred at an AoA of approximately 11° (marked by black dashed line).

For the C_L and C_D of the flapping wing, the measured force data in Section V-A were used in the calculation. Data recorded with a flapping amplitude of 50° were adopted to ensure sufficiently large amplitude of flapping. We chose the moment of the mid-stroke when θ_{flap} is zero to calculate the C_L and C_D. To extend the AoA range as much as possible, feathering amplitudes ranging from 0° to 40° were employed. The curves are depicted in Fig. 11 with solid lines.

The results demonstrate several advantages of the flapping wing compared with the case of a fixed AoA in the fixed-wing state. The lift coefficient C_L is larger than that in the fixed-wing state as expected, with a similar or lower drag coefficient C_D, until the AoA reaches approximately 33°. This larger C_L indicates that the dynamic unsteady flow in the flapping wing makes it possible to generate a larger lift force than that in the fixed-wing case. For the case of maximum thrust generation, i.e., when the AoA is 33°, the lift-to-drag ratio of the flapping wing is calculated to be 1.49, which is 1.6 times larger than that in the fixed-wing state (0.94). This high lift-to-drag ratio contributes to the forward thrust (F_x^B), as illustrated in Fig. 6(b). Moreover, the stall is postponed to an AoA of approximately 33°, and the linear operation range of the AoA is also expanded due to the postponement of the stall. The above results suggest that the flapping penguin wing could generate larger hydrodynamic forces.

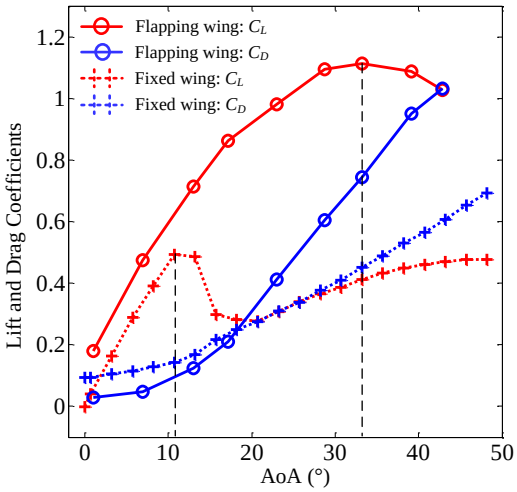

Fig. 11. Comparison of the lift and drag coefficients between the fixed-wing and flapping-wing states (black dashed lines indicate peaks in lift).

VII. Conclusion and Future Study

In this work, we first quantified the 3-D wing kinematics of a real penguin in forward horizontal swimming, revealing that it can be decomposed into flapping, feathering and pitch of the flapping axis. On this basis, we developed a 3-DoF robotic penguin wing that integrates active control on flapping and feathering angles and flapping direction at the same time. The planar shape and cross-sectional profiles of the wing were determined based on the 3-D surface morphology of the real penguin wing via 3-D scanning. To evaluate the control capability of thrust magnitude and direction, we experimentally measured the thrust while actuating the wing mechanism in a water tunnel with various motion patterns at a similar Strouhal number with real foraging penguins. As a result, it was found that a combination of smaller flapping amplitude and smaller feathering amplitude generates a lager instantaneous force, while a combination of lager flapping amplitude with lager feathering amplitude generate a larger net thrust. It was also shown that stall occurs near an AoA of 10° in the steady state; however, feathering motion can be used to effectively vary the AoA to prevent stall during flapping and maximize the net thrust (up to 7 times that without active feathering). In addition, control of the pitch angle of the robotic penguin wing was found to effectively alter the thrust direction, with a 40° variation in the pitch angle leading to a 180° change in the thrust direction.

Noted that the real penguin science is far more complicated, our research aims to create a robotic penguin wing based on the quantified basic wing kinematics of a real penguin and test its hydrodynamic thrust generation. In future studies, we will investigate cases with a wider variety of Strouhal numbers and Reynolds numbers to quantify the capabilities of robotic penguin wing. Required power and efficiency in various swimming conditions need to be evaluated as well.

Moreover, the flexibility of the wing and its hydrodynamic effect will be investigated, and a complete penguin robot will also be developed for more comprehensive studies.

ACKNOWLEDGMENTS

The authors would like to thank the staff at Nagasaki Penguin Aquarium for their kind help and cooperation in the penguin motion measurements. They would also like to thank H. Kayasuga, who contributed to the early development of the robotic penguin wing; Y. Iwasaki, Dr. M. Maeda, and T. Yamada, who contributed to the 3-D scanning and modeling of the penguin wing; and Dr. D. M. Kikuchi, for providing help in implementing the water tunnel setup.

REFERENCES

[1] W. Wang, X. Dai, L. Li, B. H. Gheneti, Y. Ding, J. Yu, and G. Xie, "Three-dimensional modeling of a fin-actuated robotic fish with multimodal swimming," *IEEE/ASME Transactions on Mechatronics*, vol. 23, no. 4, pp. 1641–1652, 2018.

[2] F. E. Fish, "Advantages of natural propulsive systems," *Marine Technology Society Journal*, vol. 47, no. 5, pp. 37–44, 2013.

[3] P. R. Bandyopadhyay, "Trends in biorobotic autonomous undersea vehicles," *IEEE Journal of Oceanic Engineering*, vol. 30, no. 1, pp. 109–139, 2005.

[4] R. K. Katzschmann, J. DelPreto, R. MacCurdy, and D. Rus, "Exploration of underwater life with an acoustically controlled soft robotic fish," *Science Robotics*, vol. 3, no. 16, p. eaar3449, 2018.

[5] S. Zhang, Y. Qian, P. Liao, F. Qin, and J. Yang, "Design and control of an agile robotic fish with integrative biomimetic mechanisms," *IEEE/ASME Transactions on Mechatronics*, vol. 21, no. 4, pp. 1846–1857, 2016.

[6] V. Kopman and M. Porfiri, "Design, modeling, and characterization of a miniature robotic fish for research and education in biomimetics and bioinspiration," *IEEE/ASME Transactions on mechatronics*, vol. 18, no. 2, pp. 471–483, 2012.

[7] S. Verma and J.-X. Xu, "Analytic modeling for precise speed tracking of multilink robotic fish," *IEEE Transactions on Industrial Electronics*, vol. 65, no. 7, pp. 5665–5672, 2017.

[8] Y. Jia and L. Wang, "Leader–follower flocking of multiple robotic fish," *IEEE/ASME Transactions on Mechatronics*, vol. 20, no. 3, pp. 1372–1383, 2014.

[9] T. Hu, K. Low, L. Shen, and X. Xu, "Effective phase tracking for bioinspired undulations of robotic fish models: A learning control approach," *IEEE/ASME Transactions on Mechatronics*, vol. 19, no. 1, pp. 191–200, 2012.

[10] L. Wen, T. Wang, G. Wu, and J. Liang, "Quantitative thrust efficiency of a self-propulsive robotic fish: Experimental method and hydrodynamic investigation," *IEEE/Asme Transactions on Mechatronics*, vol. 18, no. 3, pp. 1027–1038, 2012.

[11] F. Zhang, O. Ennasr, E. Litchman, and X. Tan, "Autonomous sampling of water columns using gliding robotic fish: Algorithms and harmful-algae-sampling experiments," *IEEE Systems Journal*, vol. 10, no. 3, pp. 1271–1281, 2015.

[12] P. Kodati, J. Hinkle, A. Winn, and X. Deng, "Microautonomous robotic ostraciiform (marco): Hydrodynamics, design, and fabrication," *IEEE Transactions on Robotics*, vol. 24, no. 1, pp. 105–117, 2008.

[13] Y.-J. Park, T. M. Huh, D. Park, and K.-J. Cho, "Design of a variable-stiffness flapping mechanism for maximizing the thrust of a bio-inspired underwater robot," *Bioinspiration & biomimetics*, vol. 9, no. 3, p. 036002, 2014.

[14] J. Yu, Z. Wu, Z. Su, T. Wang, and S. Qi, "Motion control strategies for a repetitive leaping robotic dolphin," *IEEE/ASME Transactions on Mechatronics*, vol. 24, no. 3, pp. 913–923, 2019.

[15] M. Nakashima, T. Tsubaki, and K. Ono, "Three-dimensional movement in water of the dolphin robot-control between two positions by roll and pitch combination," *Journal of robotics and mechatronics*, vol. 18, no. 3, p. 347, 2006.

[16] F. Giorgio-Serchi, A. Arienti, and C. Laschi, "Underwater soft-bodied pulsed-jet thrusters: Actuator modeling and performance profiling," *The International Journal of Robotics Research*, vol. 35, no. 11, pp. 1308–1329, 2016.

[17] F. Giorgio-Serchi, A. K. Lidtke, and G. D. Weymouth, "A soft aquatic actuator for unsteady peak power amplification," *IEEE/ASME Transactions on Mechatronics*, vol. 23, no. 6, pp. 2968–2973, 2018.

[18] Z. Shen, J. Na, and Z. Wang, "A biomimetic underwater soft robot inspired by cephalopod mollusc," *IEEE Robotics and Automation Letters*, vol. 2, no. 4, pp. 2217–2223, 2017.

[19] H. Godaba, J. Li, Y. Wang, and J. Zhu, "A soft jellyfish robot driven by a dielectric elastomer actuator," *IEEE Robotics and Automation Letters*, vol. 1, no. 2, pp. 624–631, 2016.

[20] Z. Ren, W. Hu, X. Dong, and M. Sitti, "Multi-functional soft-bodied jellyfish-like swimming," *Nature communications*, vol. 10, no. 1, pp. 1–12, 2019.

[21] J. Frame, N. Lopez, O. Curet, and E. D. Engeberg, "Thrust force characterization of free-swimming soft robotic jellyfish," *Bioinspiration & biomimetics*, vol. 13, no. 6, p. 064001, 2018.

[22] F. Hover, Ø. Haugsdal, and M. Triantafyllou, "Effect of angle of attack profiles in flapping foil propulsion," *Journal of Fluids and Structures*, vol. 19, no. 1, pp. 37–47, 2004.

[23] M. F. Platzer, K. D. Jones, J. Young, and J. C. Lai, "Flapping wing aerodynamics: progress and challenges," *AIAA journal*, vol. 46, no. 9, pp. 2136–2149, 2008.

[24] S. Heathcote, Z. Wang, and I. Gursul, "Effect of spanwise flexibility on flapping wing propulsion," *Journal of Fluids and Structures*, vol. 24, no. 2, pp. 183–199, 2008.

[25] J. S. Izraelevitz, M. Kotidis, and M. S. Triantafyllou, "Optimized kinematics enable both aerial and aquatic propulsion from a single three-dimensional flapping wing," *Physical Review Fluids*, vol. 3, no. 7, p. 073102, 2018.

[26] C. A. Hui, "Penguin swimming. i. hydrodynamics," *Physiological zoology*, vol. 61, no. 4, pp. 333–343, 1988.

[27] R. Bannasch, "Hydrodynamics of penguins-an experimental approach," *The Penguins; Ecology and Management*, pp. 141–176, 1995.

[28] J. M. Handley, A. Thiebault, A. Stanworth, D. Schutt, and P. Pistorius, "Behaviourally mediated predation avoidance in penguin prey: in situ evidence from animal-borne camera loggers," *Royal Society open science*, vol. 5, no. 8, p. 171449, 2018.

[29] Y. Y. Watanabe, K. Sato, Y. Watanuki, A. Takahashi, Y. Mitani, M. Amano, K. Aoki, T. Narazaki, T. Iwata, S. Minamikawa *et al.*, "Scaling of swim speed in breath-hold divers," *Journal of Animal Ecology*, vol. 80, no. 1, pp. 57–68, 2011.

[30] K. Sato, K. Shiomi, Y. Watanabe, Y. Watanuki, A. Takahashi, and P. J. Ponganis, "Scaling of swim speed and stroke frequency in geometrically similar penguins: they swim optimally to minimize cost of transport," *Proceedings of the Royal Society B: Biological Sciences*, vol. 277, no. 1682, pp. 707–714, 2010.

[31] B. D. Clark and W. Bemis, "Kinematics of swimming of penguins at the detroit zoo," *Journal of Zoology*, vol. 188, no. 3, pp. 411–428, 1979.

[32] W. Stoll, "Aquapenguin," Technical report, FESTO, Tech. Rep., 2009.

[33] B. Sudki, M. Lauria, and F. Noca, "Marine propulsor based on a three-degree-of-freedom actuated spherical joint," in *Proceedings of the 3rd International Symposium on Marine Propulsors*, 2013, pp. 481–485.

[34] C. Huertas-Cerdeira, "On the dynamics of flat plates in a fluid environment: A study of inverted flag flapping and caudal fin maneuvering," Ph.D. dissertation, California Institute of Technology, 2019.

[35] S.-H. Song, M.-S. Kim, H. Rodrigue, J.-Y. Lee, J.-E. Shim, M.-C. Kim, W.-S. Chu, and S.-H. Ahn, "Turtle mimetic soft robot with two swimming gaits," *Bioinspiration & biomimetics*, vol. 11, no. 3, p. 036010, 2016.

[36] C. A. Hui, "Penguin swimming. ii. energetics and behavior," *Physiological Zoology*, vol. 61, no. 4, pp. 344–350, 1988.

[37] M. Misiti, Y. Misiti, G. Oppenheim, and J.-M. Poggi, "Wavelet toolbox," *The MathWorks Inc., Natick, MA*, vol. 15, p. 21, 1996.

[38] G. K. Taylor, R. L. Nudds, and A. L. Thomas, "Flying and swimming animals cruise at a strouhal number tuned for high power efficiency," *Nature*, vol. 425, no. 6959, pp. 707–711, 2003.

[39] D. Lentink and M. H. Dickinson, "Rotational accelerations stabilize leading edge vortices on revolving fly wings," *Journal of Experimental Biology*, vol. 212, no. 16, pp. 2705–2719, 2009.

Yayi Shen received B.E. and M.E. degrees in mechanical engineering from Shanghai University, Shanghai, China, in 2013 and 2016, respectively. He received a Ph.D. degree in advanced mechanical engineering and robotics from Ritsumeikan University, Shiga, Japan, in 2019.

He is currently a postdoctoral researcher in the Aero/Aqua Biomimetics Lab, Department of Mechanical Engineering, Tokyo Institute of Technology, Tokyo, Japan. His current research interests include biomimetics, biomimetic underwater robots, and experimental fluid mechanics.

Natsuki Harada received a B.E. degree in mechanical engineering from Tokyo Institute of Technology, Tokyo, Japan, in 2020. He is currently a master student in the Aero/Aqua Biomimetics Lab. His current research interests include biomimetics, robotics, and fluid mechanics.

Sho Katagiri received B.E. and M.E. degrees in mechanical engineering from Tokyo Institute of Technology, Tokyo, Japan, in 2018 and 2020, respectively. He is currently working in Olympus Corporation, Tokyo, Japan.

Hiroto Tanaka received a B.Sc. degree in mechanical engineering from The University of Tokyo, Tokyo, Japan, in 2003; an M.Sc. degree in information science and technology from The University of Tokyo, Tokyo, Japan, in 2005; and a Ph.D. degree in information science and technology from The University of Tokyo, Tokyo, Japan, in 2008. He was a JSPS research fellow at The University of Tokyo from 2006 to 2009, a postdoctoral fellow at Harvard University from 2009 to 2011, and an Assistant Professor at Chiba University from 2011 to 2015. Currently, he is an Associate Professor in the Department of Mechanical Engineering at Tokyo Institute of Technology, Tokyo, Japan. His current research interests include fluid dynamics, biomechanics, biomimetics, and soft robotics based on flying and swimming animals.